ARTICLE

https://doi.org/10.1038/s41586-018-0298-5

Electron ptychography of 2D materials to deep sub-ångström resolution

Yi Jiang[1,6], Zhen Chen[2,6], Yimo Han[2], Pratiti Deb[1,2], Hui Gao[3,4], Saien Xie[2,3], Prafull Purohit[1], Mark W. Tate[1], Jiwoong Park[3], Sol M. Gruner[1,5], Veit Elser[1] & David A. Muller[2,5]*

Aberration-corrected optics have made electron microscopy at atomic resolution a widespread and often essential tool for characterizing nanoscale structures. Image resolution has traditionally been improved by increasing the numerical aperture of the lens (α) and the beam energy, with the state-of-the-art at 300 kiloelectronvolts just entering the deep sub-ångström (that is, less than 0.5 ångström) regime. Two-dimensional (2D) materials are imaged at lower beam energies to avoid displacement damage from large momenta transfers, limiting spatial resolution to about 1 ångström. Here, by combining an electron microscope pixel-array detector with the dynamic range necessary to record the complete distribution of transmitted electrons and full-field ptychography to recover phase information from the full phase space, we increase the spatial resolution well beyond the traditional numerical-aperture-limited resolution. At a beam energy of 80 kiloelectronvolts, our ptychographic reconstruction improves the image contrast of single-atom defects in MoS_2 substantially, reaching an information limit close to 5α, which corresponds to an Abbe diffraction-limited resolution of 0.39 ångström, at the electron dose and imaging conditions for which conventional imaging methods reach only 0.98 ångström.

The ability to image individual atoms is essential for characterizing structure and defects in 2D materials[1–3]. In scanning transmission electron microscopy (STEM), the most common technique for achieving atomic resolution is high-angle annular dark-field (ADF) imaging, which records electrons scattered through large angles to form an incoherent image. The maximum spatial information contained in

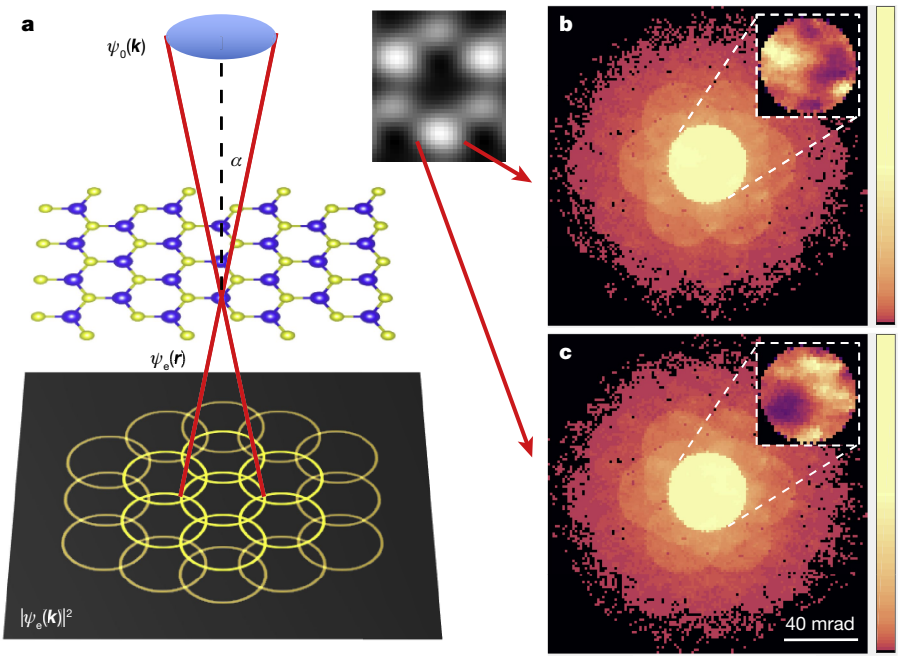

Fig. 1 | STEM imaging using the EMPAD. a, At each scan position, the incident probe ($\psi_0(\boldsymbol{k})$) is focused on the sample and the entire diffraction pattern of the exit wave ($|\psi_e(\boldsymbol{k})|^2$) is recorded by the EMPAD. The blue and yellow atoms represent molybdenum and sulfur atoms in the object plane. ψ_0 and ψ_e refer to the incident and exit wavefunctions respectively; $\boldsymbol{r}$ is the (x, y) positional coordinate in the real-space plane; and $\boldsymbol{k}$ is the (k_x, k_y) wavenumber coordinate in the conjugate momentum-space plane. **b**, **c**, Averaged diffraction pattern intensity (on a logarithmic scale) from the electron beam at the marked scan positions near a molybdenum column. Insets show the intensity (on a linear scale) of the bright-field disks. The substantial intensity differences at large scattering angles provide contrast information for ADF imaging and are essential for resolution enhancement in ptychography.

[1]Department of Physics, Cornell University, Ithaca, NY, USA. [2]School of Applied and Engineering Physics, Cornell University, Ithaca, NY, USA. [3]Department of Chemistry, Institute for Molecular Engineering, James Franck Institute, University of Chicago, Chicago, IL, USA. [4]Department of Chemistry and Chemical Biology, Cornell University, Ithaca, NY, USA. [5]Kavli Institute at Cornell for Nanoscale Science, Ithaca, NY, USA. [6]These authors contributed equally: Yi Jiang, Zhen Chen. *e-mail: david.a.muller@cornell.edu

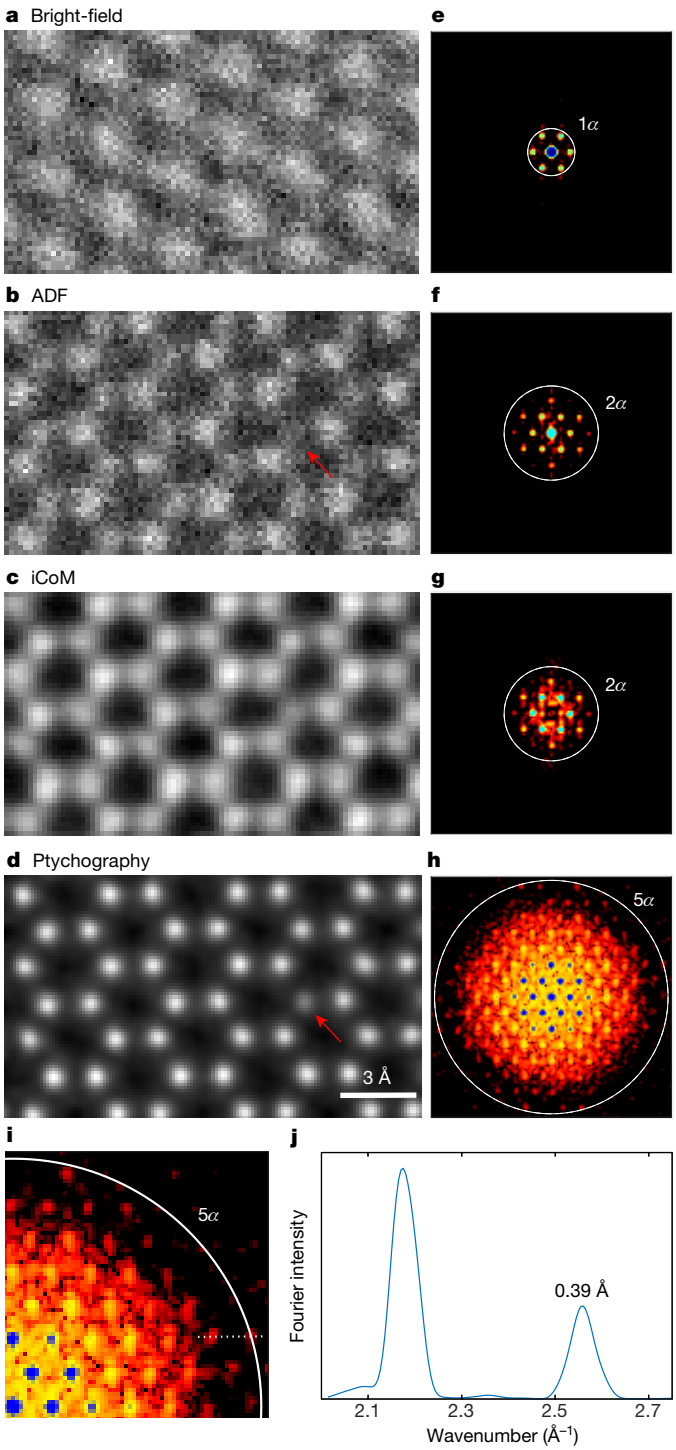

Fig. 2 | Comparison of different imaging techniques using 4D EMPAD dataset measured from monolayer MoS_2. **a**, Coherent bright-field image. **b**, Incoherent ADF image. **c**, iCoM image. **d**, Phase of the transmission function reconstructed using full-field ptychography. The red arrows indicate a sulfur monovacancy that is detectable in ptychography. **e**–**h**, False-colour diffractogram intensities (on a logarithmic scale) of the bright-field (**e**), ADF (**f**), iCoM (**g**) and full-field ptychography (**h**) images. The information limit (white circle) of ptychography is close to 5α (107 mrad); the information limits of the other imaging methods are also shown. **i**, Close-up of **h**. **j**, Line profile along the dotted horizontal white line in **i** (linear scale) across two diffraction spots. The peak at 5α corresponds to an Abbe resolution of 0.39 Å.

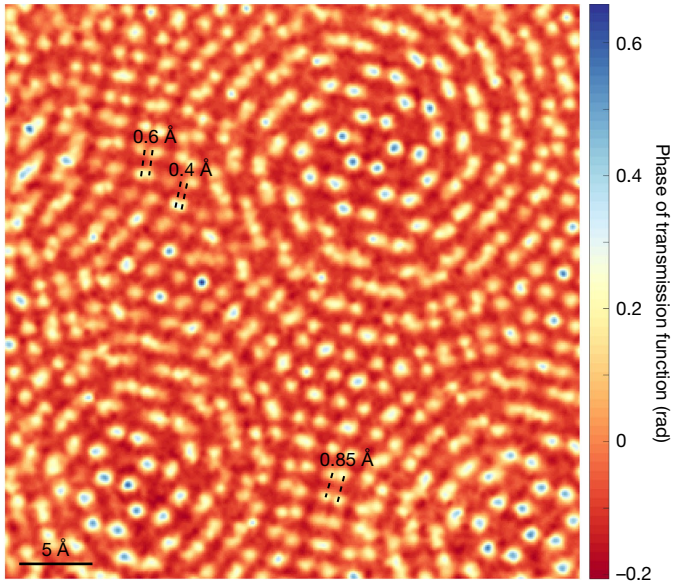

Fig. 3 | Real-space resolution test of full-field ptychography using twisted bilayer MoS_2. The two sheets are rotated by 6.8° with respect to each other, and the misregistration of the molybdenum atoms provides a range of projected distances that vary from a full bond length down to complete overlap. Atoms are still cleanly resolved at a separation of 0.85 ± 0.02 Å, with a small dip still present between atoms separated by about 0.61 ± 0.02 Å, similar to the contrast expected for the Rayleigh criterion for conventional imaging. Atom-pair peaks at 0.42 ± 0.02 Å show a 6% dip at the midpoint, suggesting that the Sparrow limit lies just below 0.4 Å. The Raleigh resolution for ADF STEM is 1.2 Å for these imaging conditions (Extended Data Fig. 3a).

an ADF image (or other incoherent imaging modes) is determined by the momentum transfer across the diameter of the probe-forming aperture—that is, twice the semi-convergence angle (α)[4,5]. Therefore, obtaining high-resolution images generally requires small wavelengths and large apertures, and the latter in turn introduces phase-distorting artefacts from geometrical and chromatic aberrations. The demonstration of practical aberration correctors[6,7] has ameliorated these phase errors substantially, and for the past decade the state-of-the-art for ADF images has reached the deep sub-ångström regime of about 0.5-Å resolution at 300 keV[8,9], which is sufficient for imaging most bulk materials. On the other hand, the characterization of 2D materials, such as single-defect detection and imaging of interface or edge structures, always requires lower beam energies (roughly 20–80 keV) to minimize knock-on damage[2,10,11]. Because lower energies imply longer electron wavelengths, the resolution of ADF imaging is reduced substantially and reaching sub-ångström resolution is possible only with specialized correctors that correct both geometric and chromatic aberrations or with monochromatic electron beams[12,13]. Moreover, ionization damage, which cannot be avoided by lowering the beam voltage, also restricts the electron dose applied to the sample, limiting the ultimately achievable signal-to-noise ratio[14], further reducing image resolution and contrast.

However, it has long been recognized that the information limit set by diffractive optics is not an ultimate limit[15]. There is phase information encoded throughout a diffraction pattern formed from a localized electron beam, in the form of interference patterns between overlapping scattered beams (Fig. 1a). As the incident localized beam is scanned, this phase information and hence the interference patterns change in a predictable manner that can be used to retrieve the phase differences—an approach known as ptychography[16–18]. Although originally conceived to solve the phase problem in crystallography, modern ptychography is equally applicable to non-crystalline structures[19–22] and has received renewed attention as a dose-efficient technique[23,24] for recovering the projected potential of thin materials, with modifications for measuring finite-thickness and three-dimensional samples[25,26]. In principle, the resolution is limited by the largest scattering angle at which meaningful information can still be recorded; however, because

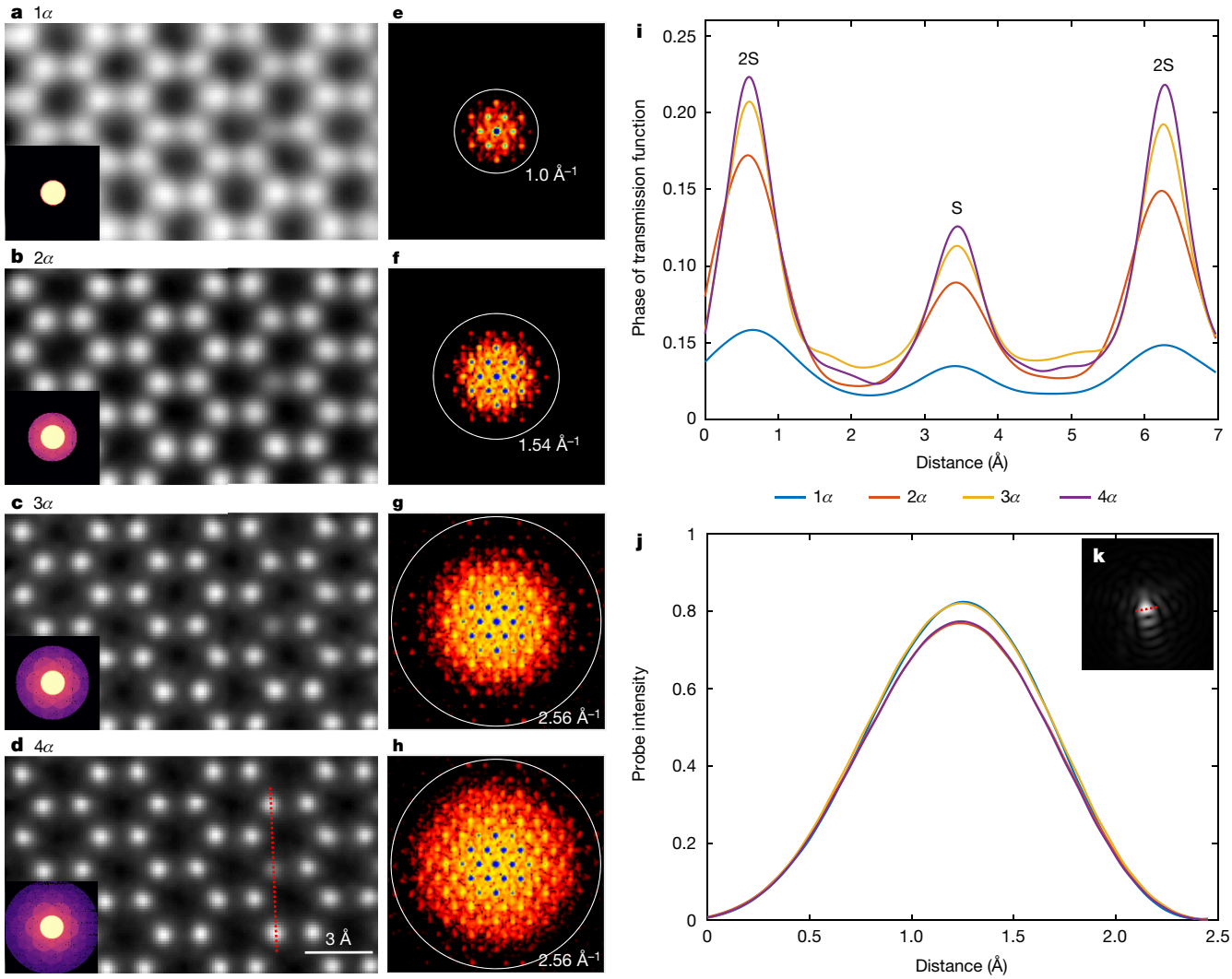

Fig. 4 | Ptychographic reconstructions using data with different cutoff angles. a–d, Ptychographic reconstructions using electrons collected using cutoffs of 1–4 times the aperture size (α). The averaged diffraction patterns are shown in the lower-left corner of each image. **e–h**, False-colour diffractograms (on a logarithmic scale) of the reconstructions in **a–d**. The white circles indicate the information limit. **i**, Line profiles across three sulfur columns (indicated by the vertical red dashed line in **d**). The columns containing two sulfur atoms are labelled 2S; the column with one sulfur atom is labelled S. **j**, Line profiles across the reconstructed probe function (dashed line in **k**) at different cutoffs. **k**, Probe profile reconstructed by ptychography using the dataset with a 4α cutoff.

electron-scattering form factors have a very strong angular dependence, the signal falls rapidly with scattering angle, so a detector with high dynamic range and sensitivity is required to exploit this information.

Ptychography has been widely adopted for light[27] and X-ray[19,28] applications, but the technique is still underexplored in transmission electron microscopy, in large part because of the detector challenges. Traditional electron cameras such as charge-coupled devices (CCDs) and pixelated detectors have been hampered by slow readout speed or poor dynamic range. Previous work[23,29–35] has mainly made use of electrons only within the bright-field disk; therefore, the image resolution did not overcome the 2α limit imposed by the physical aperture. The first attempt[17] at demonstrating super-resolution ptychography involved phasing the Fourier coefficients of silicon out to the (400) reflection to reconstruct the unit cell with a resolution of 1.36 Å. However, this result determined only structure factors, limiting its application to periodic crystalline structures. A more recent demonstration[36] for a lower-resolution scanning electron microscope equipped with a CCD camera showed that the resolution of iterative ptychographic reconstructions can be improved when using information at higher scattering angles.

There are three challenges to improving resolution and dose efficiency to the point needed to advance beyond the current state-of-the-art diffractive imaging. First, a detector must be able to record the full range of scattered intensities without introducing non-linear distortions or saturating the central beam. Second, the detector must not only possess single-electron sensitivity, but also retain a high detective quantum efficiency when summing over the large ranges of empty pixels at high scattering angles. Third, each diffraction pattern must be recorded rapidly enough that the full image is not sensitive to drift and instabilities in the microscope, which usually leaves only a few minutes to record a full four-dimensional (4D) dataset. The combination of the first and third conditions poses an additional constraint that the detector must also have a high dynamic current range. Therefore, it is not sufficient to count single electrons for a long time at a low beam current; instead, large currents per pixel need to be recorded in very short times. Most pulse-counting methods are limited to about 2–10 MHz by the transit time of the electron cloud through the silicon detector. This translates to 0.3–1.6 pA per pixel, although few systems reach this limit. Instead, to keep nonlinearities below 10%, a limit of 0.03 pA per pixel is more typical[37]. Direct charge integration in a CCD geometry is even more limited by the well depth, to about 20 electrons per pixel per frame. At a 1-kHz frame, this corresponds to 0.003 pA per pixel—a limit at which single-frame Poisson statistics would then be below the Rose criterion for contrast detectability[38].

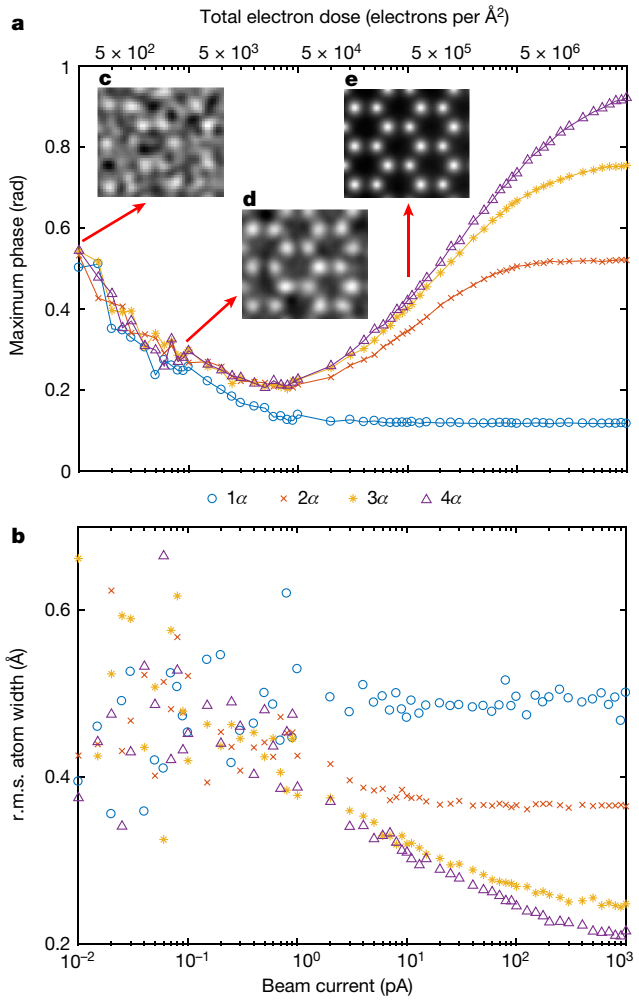

Fig. 5 | Simulation study of full-field ptychography as a function of cutoff angle and beam current. a, **b**, Reconstruction resolution evaluated by the maximum range of the reconstructed phase (**a**) and the root-mean-square (r.m.s.) width of the molybdenum atom defined by the standard deviation of a fitted Gaussian (**b**). At large electron doses, the resolution is determined by the maximum detector angle. As current decreases, the resolution is instead limited by the Poisson noise. **c**–**e**, Reconstructed phase maps using diffraction patterns with 4α cutoff at beam currents of 0.01 pA (**c**), 0.1 pA (**d**) and 10 pA (**e**), as indicated by the arrows. The increase in the phase range and the decrease of the r.m.s. atom width at large dose (more than 1 pA) is a measure of the resolution improvement, but the increase in the phase range at low dose (less than 1 pA) reflects increasingly large noise fluctuations in the reconstructions, which are also evident in the increased variations of the r.m.s. atom width.

To overcome these challenges, we developed an electron microscope pixel-array detector (EMPAD)[39] that is capable of recording all the transmitted electrons with sufficient sensitivity and speed to provide a complete ptychographic reconstruction. Our EMPAD design has a high dynamic range of 1,000,000:1 while preserving single-electron sensitivity with a signal-to-noise ratio of 140 for a single electron at 200 keV[39]. The detector retains a good performance from 20 keV to 300 keV. Here we operate at 80 keV, at which the signal-to-noise ratio per pixel is 50 for a single electron, the detective quantum efficiency is 0.96 and the maximum beam current per pixel is 5 pA. By using essentially all of the electrons collected (99.95% of the transmitted beam, as determined using multi-slice simulations), with a full 4D dataset acquired in typically a minute, our full-field ptychographic reconstructions roughly double the image resolution compared to the highest-resolution conventional single-channel imaging modes, such integrated centre-of-mass (iCoM)[40,41] and ADF STEM.

Data acquisition and reconstruction

In Fig. 1a we show a schematic of the experimental configuration with the EMPAD. To minimize radiation damage, a monolayer of MoS_2 is imaged at a primary beam energy of 80 keV. At each (x, y) scan position, the EMPAD records a diffraction pattern (k_x, k_y) from the convergent probe, thus forming a 4D dataset (x, y, k_x, k_y). In Fig. 1b, c we show averaged diffraction patterns corresponding to two positions near a single molybdenum column. Supplementary Videos 1 and 2 show continuous evolutions of averaged and raw diffraction patterns, respectively, at various scan positions, where, compared to Fig. 1b, c it is easier to observe the intensity variations in the overlaps between the higher-order diffraction disks that occur as the relative phase of the interfering beams changes with position. The considerable changes in the distribution outside the central disk provides essential contrast information in ADF images; the resolution improvement in full-field ptychography over previous bright-field ptychographic methods stems from exploiting the phase information encoded in the contrast between overlapping higher-order disks. The angle-averaged radial distribution function of the position-averaged diffraction pattern (Extended Data Fig. 1) shows a four-orders-of-magnitude intensity range for our dataset. The reconstruction algorithm is implemented using the extended ptychographic iterative engine (ePIE) algorithm[20,42], which reconstructs the transmission function iteratively and refines the probe function to accommodate aberrations and noise. We also compare our performance to the simpler Wigner-distribution deconvolution (WDD)[43], which in its simplest form assumes a known probe function and uses the information within the central disk, and shows a similar performance to using ePIE on only the central disk (that is, with a cutoff α) or iCoM imaging. In principle, WDD could also utilize the dark-field signal and surpass the aperture-limited resolution if a proper de-noising strategy is applied[43,44].

The 4D EMPAD data can generate all elastic imaging modes for benchmarking from the same dataset, including coherent bright-field, iCoM and ADF modes. As shown in Fig. 2a, e, the coherent bright-field image has the poorest resolution (restricted to within α, as expected). The incoherent ADF image (Fig. 2b, f) doubles the information limit (from α to 2α), but is limited by a low signal-to-noise ratio and residual probe aberrations. Although the iCoM image is less noisy, its resolution is still within 2α (Fig. 2g) because the structural information is influenced by the incident probe via convolution. By contrast, full-field ptychography recovers the phase of the transmission function directly (Fig. 2d) and achieves an information limit of 5α (Fig. 2h). Noise artefacts are also reduced substantially and the light-atom sulfur monovacancy (indicated by red arrows) is resolved more clearly. In Fig. 2i, j we show an enlarged section of the Fourier intensity map from the ptychographic reconstruction and a line profile across a diffraction spot at the 5α limit, demonstrating an estimated Abbe resolution[45] of 0.39 Å or better (there are higher-order spots of weaker intensity but they are not as uniform in all directions). For comparison, with our electron optical conditions, the expected Abbe resolution for conventional incoherent imaging modes such as ADF STEM is 2α or 0.98 Å.

A second measure of spatial resolution is the minimum resolvable distance between two atoms. For 2D materials, this measure is complicated by the fact that it requires atoms to be spaced closer than the shortest known bond lengths. To accomplish this test, we use a twisted bilayer sample of two MoS_2 sheets rotated by 6.8° with respect to each other. This effectively creates an incommensurate atomic moiré pattern, which provides projected Mo–Mo atomic distances that vary from a full bond length to fully superimposed atoms, with many intermediate distances across the incommensurate moiré quasi-periodicity of 28 Å (see, for example, Fig. 1c of ref. [46]). In Fig. 3 we show the ptychographic reconstruction across a moiré supercell, in which atomic columns midway between the aligned regions are resolved as separate atoms at 0.85 ± 0.02 Å. The dominant uncertainty here, and in our other distance measurements, is the systematic error from scan distortions rather than random errors from counting statistics. The dip between adjacent columns can still be seen at 0.60 ± 0.02 Å—close to the Rayleigh limit

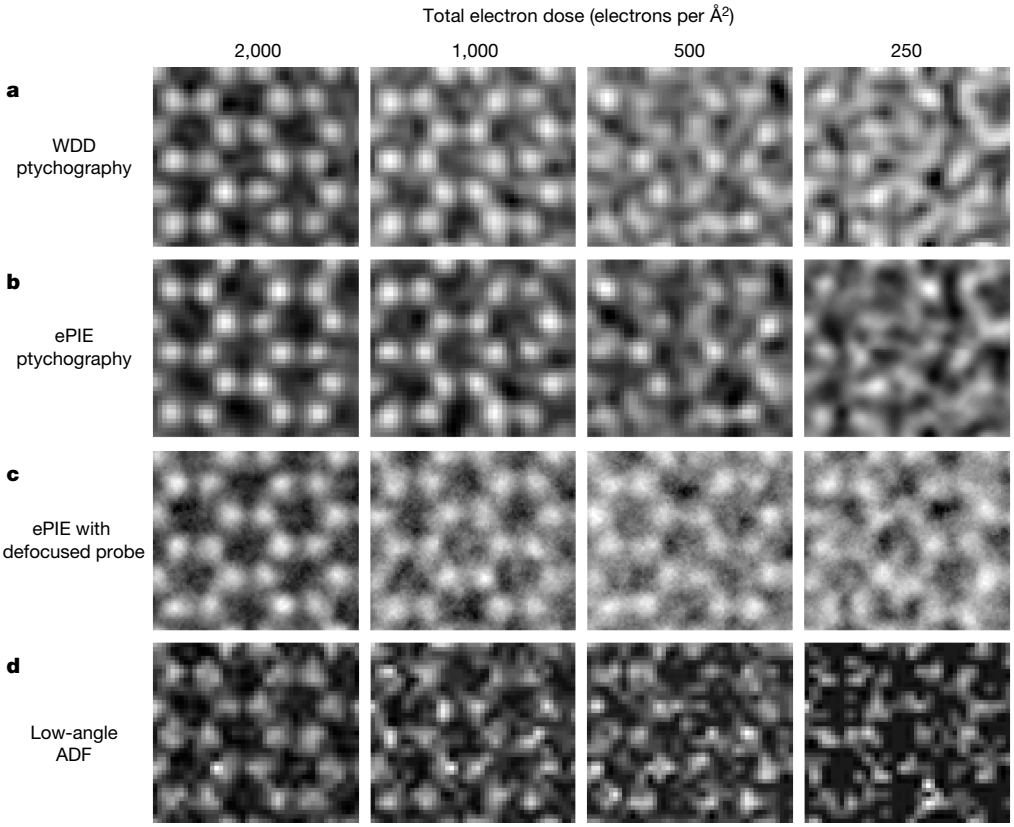

Fig. 6 | Comparison between ptychographic techniques and low-angle ADF imaging at low electron doses. a, **b**, Ptychographic reconstructions of simulated data with an in-focused probe, using the WDD (**a**) and ePIE (**b**) methods. **c**, ePIE reconstructions of data with a large defocused probe. **d**, Low-angle ADF image (integrating from 1α to 4α) using the same simulated dataset as for **a** and **b**. The defocused ePIE approach (**c**) shows a dose advantage over the other two ptychography approaches (**a**, **b**) by a factor of roughly two or better, and over low-angle ADF imaging (**d**)—currently the optimal single-channel imaging method for 2D materials—by a factor of roughly four.

for resolution. Atom-pair peaks measured at 0.42 ± 0.02 Å show a 6% dip at the midpoint (line profiles through atoms pairs are shown in Extended Data Figs. 2, 3). From a rigid model structure of the rotated bilayer, assuming that no relaxation occurs (even though some probably does), the model separations for the atom pairs marked in Fig. 3 are predicted to be 0.87 Å, 0.60 Å and 0.36 Å. Although not all atoms can be reconstructed because of scan noise, we have multiple moiré repeats to distinguish random from systematic errors. Ignoring source-size contributions, the expected Rayleigh limit for an incoherent imaging mode for this experimental condition is 1.2 Å, and many atom pairs are completely unresolvable in the ADF image (Extended Data Fig. 3a). Our full-field ptychographic reconstruction demonstrates double the Rayleigh resolution compared to conventional 2α imaging methods. Moreover, some closely spaced atoms lose the central dip at just below 0.40 Å (the Sparrow[4] criterion for resolution), close to the Abbe limit estimated from Fig. 2.

To understand how dark-field electrons contribute to resolution improvement, we performed additional reconstructions using diffraction patterns with outer cutoff angles varying from one to four times the aperture size (1α–4α). As shown in Fig. 4a–h, when using only the central bright-field disk (1α), the reconstructed phase (Fig. 4a) has a relatively low resolution, similar to that of the ADF and iCoM images. As the cutoff increases, atoms become sharper and more clearly resolved (Fig. 4a–d). Higher-spatial-frequency information also appears in the diffractograms (Fig. 4e–h). Beyond 3α, where there are fewer scattered electrons, the improvements become less obvious and the reconstruction is limited mainly by the electron dose. As discussed in more detail in the following section, increasing the collection angle beyond the point at which there is meaningful signal in the diffraction pattern does not introduce high-spatial-frequency artefacts. Instead, the reconstruction retains its limiting form. We note that the reconstructed amplitude of the transmission function also shows the atomic structure of MoS_2. The amplitude modulations are weak, suggesting that the specimen is close to a pure phase object (Extended Data Fig. 4).

As a test of linearity, Fig. 4i shows that the phase at the position of the sulfur monovacancy, where only one sulfur atom is present, is about half of the phase shift of the two-sulfur sites, validating the strong-phase approximation and ePIE reconstruction for these thin 2D materials. That the reconstructed probes (Fig. 4j, k) have similar shapes at different cutoffs also indicates that it is the dark-field electrons that contribute to resolution improvement. The asymmetric probe shape is due to residual aberrations and agrees with measurements using the singular-value-decomposition approach[23].

Influence of electron dose

We explored the potential limits of full-field ptychography further using simulated datasets for a wide range of collection angles and beam currents, including cases where the cutoff is extended beyond most of the scattered electrons and where the dose is too small for a stable reconstruction to be achieved. We evaluate the image quality by both the range of the reconstructed phase and the root-mean-square width of the molybdenum atoms measured from the standard deviation of a Gaussian fit. These measures capture the trends in the height and width of the atom peak, respectively. At high dose, the ultimate information limit of the ptychographic reconstruction is expected to be twice the cutoff angle—that is, 8α for a 4α cutoff. In practice, as shown in Fig. 5, ptychographic reconstructions are influenced mainly by the electron dose, and these limits are not reached for the larger cutoffs. There is only a slight improvement between the 3α and 4α cutoff at a typical operating beam current (1–50 pA), in agreement with the experimental data in Fig. 4. If the beam current is too low (for example, 0.01 pA, which corresponds to a dose of 260 electrons

per Å^2), atoms become distorted with reduced image resolution, but some of the overall structure of MoS_2 is still recognizable (Fig. 5c). As the beam current increases, the influence of Poisson noise becomes less important because there are sufficient electrons scattered into high angles to provide interference between higher-order lattice planes. At higher doses, the resolution of the ptychographic reconstruction benefits more fully from the increased maximum collection angle. For large collection angles and high doses, a diminishing return eventually sets in, with the resolution scaling logarithmically with the dose, suggesting that in practice the resolution will ultimately be limited by dose rather than the finite size of the scattering potential (root-mean-square width of about 0.1 Å) or thermal vibrations. Because the EMPAD has a high detective quantum efficiency, increasing the cutoff angle beyond where there is signal does not compromise resolution or introduce additional artefacts, as demonstrated by the fact that all curves in Fig. 5a collapse to the same trend as the beam current decreases.

In Fig. 6 we compare the performance of ePIE and WDD ptychographic reconstructions at low electron dose. Using the same datasets, simulated with a small in-focused probe, both methods yield similar results and can achieve atomic resolution at around 500 electrons per Å^2. On the other hand, using a large defocused probe, the ePIE technique can improve reconstruction quality beyond that of WDD (Fig. 6c). Overall, ptychographic reconstructions are more dose-efficient than are low-angle ADF reconstructions (integrating from 1α upwards; Fig. 6d); low-angle ADF is currently the most dose-efficient single-channel STEM imaging mode for single-atom detection[47]. For a more typical range of ADF angles, such as the experimental data of Fig. 2b, the effects are more pronounced (see, for example, Fig. 2d). As shown in Extended Data Fig. 5, the advantage of ptychography over ADF imaging becomes more noticeable for materials with lighter elements, such as graphene.

Discussion

In addition to the beam current and detector configuration required for high-resolution ptychographic reconstruction, other practical sources of errors such as sample contamination and scanning drift may cause distortions and reduce reconstruction quality. However, we have found that full-field ptychography outperforms all other techniques that we have tested under the same conditions (Extended Data Fig. 6). By incorporating other physical constraints and prior knowledge, we envisage that more advanced reconstruction strategies, when applied to full-field electron ptychography data, could compensate for inaccurate scan positions or make allowances for thick specimens with strong dynamic scattering.

In summary, we have demonstrated that with the entire distribution of scattered electrons collected by the EMPAD, full-field ptychography greatly enhances image resolution and contrast compared to traditional electron-imaging techniques, even at low beam voltages. With our improved detector, atomic-scale ptychographic reconstructions are no longer restricted by the aperture size. Instead, image quality is determined by the electron dose and collection angle. Our technique provides an efficient tool for unveiling sub-ångström features of 2D or dose-sensitive materials. Combined with the ultralow-voltage aberration-corrected microscopes that have recently been developed, it has the potential to tackle currently hard problems such as direct imaging of lattice displacements in twisted-layer structures or of structural distortions around single-atom dopants and vacancies, and even three-dimensional tomography.

Online content

Any Methods, including any statements of data availability and Nature Research reporting summaries, along with any additional references and Source Data files, are available in the online version of the paper at https://doi.org/10.1038/s41586-018-0298-5.

Received: 14 January 2018; Accepted: 24 May 2018;
Published online 18 July 2018.

1. Meyer, J. C., Girit, C. O., Crommie, M. F. & Zettl, A. Imaging and dynamics of light atoms and molecules on graphene. *Nature* **454**, 319–322 (2008).
2. Krivanek, O. L. et al. Atom-by-atom structural and chemical analysis by annular dark-field electron microscopy. *Nature* **464**, 571–574 (2010).
3. Huang, P. Y. et al. Grains and grain boundaries in single-layer graphene atomic patchwork quilts. *Nature* **469**, 389–392 (2011).
4. Sparrow, C. M. On spectroscopic resolving power. *Astrophys. J.* **44**, 76–86 (1916).
5. Black, G. & Linfoot, E. H. Spherical aberration and the information content of optical images. *Proc. R. Soc. Lond. A* **239**, 522–540 (1957).
6. Haider, M. et al. Electron microscopy image enhanced. *Nature* **392**, 768–769 (1998).
7. Batson, P. E., Dellby, N. & Krivanek, O. L. Sub-ångström resolution using aberration corrected electron optics. *Nature* **418**, 617–620 (2002).
8. Erni, R., Rossell, M. D., Kisielowski, C. & Dahmen, U. Atomic-resolution imaging with a sub-50-pm electron probe. *Phys. Rev. Lett.* **102**, 096101 (2009).
9. Sawada, H. et al. STEM imaging of 47-pm-separated atomic columns by a spherical aberration-corrected electron microscope with a 300-kV cold field emission gun. *J. Electron Microsc.* **58**, 357–361 (2009).
10. Kaiser, U. et al. Transmission electron microscopy at 20kV for imaging and spectroscopy. *Ultramicroscopy* **111**, 1239–1246 (2011).
11. Meyer, J. C. et al. Accurate measurement of electron beam induced displacement cross sections for single-layer graphene. *Phys. Rev. Lett.* **108**, 196102 (2012).
12. Sawada, H., Sasaki, T., Hosokawa, F. & Suenaga, K. Atomic-resolution STEM imaging of graphene at low voltage of 30 kV with resolution enhancement by using large convergence angle. *Phys. Rev. Lett.* **114**, 166102 (2015).
13. Linck, M. et al. Chromatic aberration correction for atomic resolution TEM imaging from 20 to 80 kV. *Phys. Rev. Lett.* **117**, 076101 (2016).
14. Henderson, R. The potential and limitations of neutrons, electrons and X-rays for atomic resolution microscopy of unstained biological molecules. *Q. Rev. Biophys.* **28**, 171–193 (1995).
15. Gabor, D. A new microscopic principle. *Nature* **161**, 777–778 (1948).
16. Hoppe, W. Beugung im inhomogenen Primärstrahlwellenfeld. I. Prinzip einer Phasenmessung von Elektronenbeugungsinterferenzen. *Acta Crystallogr. A* **25**, 495–501 (1969).
17. Nellist, P. D., McCallum, B. C. & Rodenburg, J. M. Resolution beyond the 'information limit' in transmission electron microscopy. *Nature* **374**, 630–632 (1995).
18. Nellist, P. D. & Rodenburg, J. M. Electron ptychography. I. Experimental demonstration beyond the conventional resolution limits. *Acta Crystallogr. A* **54**, 49–60 (1998).
19. Thibault, P. et al. High-resolution scanning X-ray diffraction microscopy. *Science* **321**, 379–382 (2008).
20. Maiden, A. M. & Rodenburg, J. M. An improved ptychographical phase retrieval algorithm for diffractive imaging. *Ultramicroscopy* **109**, 1256–1262 (2009).
21. Thibault, P. & Menzel, A. Reconstructing state mixtures from diffraction measurements. *Nature* **494**, 68–71 (2013).
22. Li, P., Edo, T. B. & Rodenburg, J. M. Ptychographic inversion via Wigner distribution deconvolution: noise suppression and probe design. *Ultramicroscopy* **147**, 106–113 (2014).
23. Yang, H. et al. Simultaneous atomic-resolution electron ptychography and Z-contrast imaging of light and heavy elements in complex nanostructures. *Nat. Commun.* **7**, 12532 (2016).
24. Pelz, P. M., Qiu, W. X., Bücker, R., Kassier, G. & Miller, R. J. D. Low-dose cryo electron ptychography via non-convex Bayesian optimization. *Sci. Rep.* **7**, 9883 (2017).
25. Maiden, A. M., Humphry, M. J. & Rodenburg, J. M. Ptychographic transmission microscopy in three dimensions using a multi-slice approach. *J. Opt. Soc. Am. A* **29**, 1606–1614 (2012).
26. Gao, S. et al. Electron ptychographic microscopy for three-dimensional imaging. *Nat. Commun.* **8**, 163 (2017).
27. Rodenburg, J. M., Hurst, A. C. & Cullis, A. G. Transmission microscopy without lenses for objects of unlimited size. *Ultramicroscopy* **107**, 227–231 (2007).
28. Rodenburg, J. M. et al. Hard-X-ray lensless imaging of extended objects. *Phys. Rev. Lett.* **98**, 034801 (2007).
29. Hüe, F., Rodenburg, J. M., Maiden, A. M., Sweeney, F. & Midgley, P. A. Wave-front phase retrieval in transmission electron microscopy via ptychography. *Phys. Rev. B* **82**, 121415 (2010).
30. Hüe, F., Rodenburg, J. M., Maiden, A. M. & Midgley, P. A. Extended ptychography in the transmission electron microscope: possibilities and limitations. *Ultramicroscopy* **111**, 1117–1123 (2011).
31. Putkunz, C. T. et al. Atom-scale ptychographic electron diffractive imaging of boron nitride cones. *Phys. Rev. Lett.* **108**, 073901 (2012).
32. D'Alfonso, A. J. et al. Deterministic electron ptychography at atomic resolution. *Phys. Rev. B* **89**, 064101 (2014).
33. Pennycook, T. J. et al. Efficient phase contrast imaging in STEM using a pixelated detector. Part 1: experimental demonstration at atomic resolution. *Ultramicroscopy* **151**, 160–167 (2015).
34. Yang, H. et al. Electron ptychographic phase imaging of light elements in crystalline materials using Wigner distribution deconvolution. *Ultramicroscopy* **180**, 173–179 (2017).
35. Wang, P., Zhang, F., Gao, S., Zhang, M. & Kirkland, A. I. Electron ptychographic diffractive imaging of boron atoms in LaB_6 crystals. *Sci. Rep.* **7**, 2857 (2017).

36. Humphry, M. J., Kraus, B., Hurst, A. C., Maiden, A. M. & Rodenburg, J. M. Ptychographic electron microscopy using high-angle dark-field scattering for sub-nanometre resolution imaging. *Nat. Commun.* **3**, 730 (2012).
37. Frojdh, E. et al. Count rate linearity and spectral response of the Medipix3RX chip coupled to a 300μm silicon sensor under high flux conditions. *J. Instrum.* **9**, C04028 (2014).
38. Rose, A. *Vision Human and Electronic* Ch. 1 (Plenum Press, New York, 1949).
39. Tate, M. W. et al. High dynamic range pixel array detector for scanning transmission electron microscopy. *Microsc. Microanal.* **22**, 237–249 (2016).
40. Close, R., Chen, Z., Shibata, N. & Findlay, S. D. Towards quantitative, atomic-resolution reconstruction of the electrostatic potential via differential phase contrast using electrons. *Ultramicroscopy* **159**, 124–137 (2015).
41. Lazić, I., Bosch, E. G. T. & Lazar, S. Phase contrast STEM for thin samples: integrated differential phase contrast. *Ultramicroscopy* **160**, 265–280 (2016).
42. Maiden, A. M., Humphry, M. J., Zhang, F. & Rodenburg, J. M. Superresolution imaging via ptychography. *J. Opt. Soc. Am. A* **28**, 604–612 (2011).
43. Rodenburg, J. M. & Bates, R. H. T. The theory of super-resolution electron microscopy via Wigner-distribution deconvolution. *Philos. Trans. R. Soc. Lond. A* **339**, 521–553 (1992).
44. Lee, J. & Barbastathis, G. Denoised Wigner distribution deconvolution via low-rank matrix completion. *Opt. Express* **24**, 20069–20079 (2016).
45. Abbe, E. The relation of aperture and power in the microscope. *J. R. Microsc. Soc.* **2**, 300–309 (1882).
46. van der Zande, A. M. et al. Tailoring the electronic structure in bilayer molybdenum disulfide via interlayer twist. *Nano Lett.* **14**, 3869–3875 (2014).
47. Hovden, R. & Muller, D. A. Efficient elastic imaging of single atoms on ultrathin supports in a scanning transmission electron microscope. *Ultramicroscopy* **123**, 59–65 (2012).

Acknowledgements Y.J. and V.E. acknowledge support from DOE grant DE-SC0005827. Z.C. and D.A.M. are supported by the PARADIM Materials Innovation Platform in-house programme by NSF grant DMR-1539918. We acknowledge the electron microscopy facility and support for Y.H. from the NSF MRSEC programme (DMR 1719875) and NSF MRI grant DMR-1429155. H.G., S.X. and J.P. acknowledge additional support from AFOSR MURI (FA9550-16-1-003) and UChicago NSF MRSEC programme (DMR 1420709). Detector development at Cornell was supported by the Kavli Institute at Cornell for Nanoscale Science and DOE grant DE-SC0017631 to S.M.G. We thank K. Nguyen, P. Huang, M. Humphry and P. Nellist for discussions and B. Jiang from Thermo Scientific for help during the initial experiments.

Reviewer information *Nature* thanks J. Rodenburg and the other anonymous reviewer(s) for their contribution to the peer review of this work.

Author contributions Experiments were performed and designed by Z.C., Y.H. and D.A.M. Y.J. contributed to data analysis and ptychographic reconstruction, with support from V.E. Sample preparation was done by P.D. and Y.H., from MoS_2 thin films synthesized by H.G., S.X. and J.P. EMPAD was optimized by P.P., M.W.T. and S.M.G. All authors discussed the results and implications throughout the investigation. All authors have approved the final version of the manuscript.

Competing interests Cornell University has licensed the EMPAD hardware to Thermo Scientific.

Additional information

Extended data is available for this paper at https://doi.org/10.1038/s41586-018-0298-5.
Supplementary information is available for this paper at https://doi.org/10.1038/s41586-018-0298-5.
Reprints and permissions information is available at http://www.nature.com/reprints.

Correspondence and requests for materials should be addressed to D.A.M.

METHODS

EMPAD data acquisition. The 4D dataset of monolayer MoS_2 was taken using an aberration-corrected FEI Titan with 8.2-pA beam current, 80-keV beam energy and 21.4-mrad aperture size, with the dose limited by the radiation resistance of the sample. The EMPAD has 128 × 128 pixels and a readout speed of 0.86 ms per frame. The exposure time was set to 1 ms per frame in all experiments. 51 × 87 diffraction patterns with a scan step size of 0.21 Å were used to generate bright-field, ADF and iCoM images in Fig. 2a–c. The ADF image was integrated from 64.2 mrad (3α) to 84.6 mrad (4α). Higher angles did not add important contributions to the signal. The dataset of twisted MoS_2 in Fig. 3 was taken with the same beam conditions except for a 10.1-pA beam current. 68 × 68 diffraction patterns with a scan step size of 0.59 Å were used for ptychographic reconstruction.

Ptychographic reconstructions. Before reconstruction, all diffraction patterns are padded with zeros to a total size of 256 × 256 and thus the pixel size in the reconstructed phase is 0.12 Å per pixel. The ePIE method[20] is implemented with modifications to exclude bad pixels in the diffraction patterns. The algorithm uses a multiplicative approximation, which is a generalization of the strong-phase approximation, allowing for both a strong phase object and a variable amplitude term. It aims to minimize the Euclidian distance between reconstructed and measured diffraction patterns. In general, the convergence of reconstructions depends on the number of iterations and update parameters for the transmission function and the probe function. Because experimental data contain noise and other sources of errors, fast convergence may introduce noisy artefacts and reduce reconstruction quality[48,49]. To alleviate this problem, we used a small update parameter (0.1) for the transmission function and limited the reconstruction of the probe function to data taken in areas with minimal contamination. For our experimental conditions, with cutoff angle $\theta_{max} = 80$ mrad, the thickness limit dz for treating the sample as a projected potential and neglecting beam propagation is estimated to be $dz = \lambda/[2\sin^2(\theta_{max}/2)] \approx 1.3$ nm[50], which is larger than the thicknesses of both the monolayer MoS_2 (3.1 Å) and the bilayer MoS_2 (9.8 Å).

Fourier resolution estimate. All diffractograms (Fourier intensity) of bright-field, ADF, iCoM and ptychography reconstructions in Fig. 2 were calculated from images constructed from 128 × 128 diffraction patterns (see Extended Data Fig. 6). To visualize diffraction spots, a periodic and smooth decomposition[51] was applied to images to reduce artefacts caused by edge discontinuities. Next, the real-space image was multiplied by a Gaussian function, making the diffraction spots slightly larger and thus more visible. The Fourier intensity was rescaled to enhance the intensity of higher-order spots for better visualization.

4D data simulation. All datasets used for dose-cutoff simulations were generated by the μSTEM software[52], which models the atomic potential using scattering factors given in ref. [53]. For the in-focused probe, 21 × 24 diffraction patterns with a 0.45-Å scan step size were simulated at 80-keV beam energy and with 21.4-mrad aperture size. The thermal diffuse scattering effect was included with the frozen-phonon approximation. The diffraction patterns were further corrupted with Poisson noise determined by the simulated beam dose. Extended Data Fig. 7 shows selected ePIE reconstructions at different beam currents (0.01–100 pA) and cutoff angles (1α–4α). Simulations (Fig. 6c) of the large probe profile used a 80-nm defocus and 10.04-Å scan step size.

Effect of chromatic aberrations. Ptychography is less sensitive to chromatic blur than is direct phase imaging[54], but it is still sensitive, especially at low doses. 4D datasets including chromatic aberrations were simulated for a Gaussian energy spread with full-width at half-maximum of $\Delta E = 1.1$ eV, a chromatic aberration coefficient of $C_c = 1.72$ mm and a beam energy of 80 keV. Two different probe-forming aperture sizes, 21.4 mrad and 35 mrad, were chosen to reflect conditions under which chromatic blur is moderate and strong, respectively. The dose dependence of ePIE reconstructions for datasets with and without chromatic aberration is shown in Extended Data Fig. 8. Under the experimental conditions, the influence of chromatic aberration is visually negligible. At lower doses, the larger chromatic blur for the larger aperture leads to a worse reconstruction.

Data availability. All relevant data are available from the corresponding author on request.

Code availability. Code developed at Cornell, including visualization software for 4D datasets, is available from the corresponding author on request. μSTEM was developed at the University of Melbourne and can be downloaded from http://tcmp.ph.unimelb.edu.au/mustem/muSTEM.html.

48. Zuo, C., Sun, J. & Chen, Q. Adaptive step-size strategy for noise-robust Fourier ptychographic microscopy. *Opt. Express* **24**, 20724–20744 (2016).
49. Maiden, A., Johnson, D. & Li, P. Further improvements to the ptychographical iterative engine. *Optica* **4**, 736–745 (2017).
50. Suzuki, A. et al. High-resolution multislice X-ray ptychography of extended thick objects. *Phys. Rev. Lett.* **112**, 053903 (2014).
51. Hovden, R., Jiang, Y., Xin, H. L. & Kourkoutis, L. F. Periodic artifact reduction in Fourier transforms of full field atomic resolution images. *Microsc. Microanal.* **21**, 436–441 (2015).
52. Allen, L. J., D'Alfonso, A. J. & Findlay, S. D. Modelling the inelastic scattering of fast electrons. *Ultramicroscopy* **151**, 11–22 (2015).
53. Waasmaier, D. & Kirfel, A. New analytical scattering-factor functions for free atoms and ions. *Acta Crystallogr. A* **51**, 416–431 (1995).
54. Nellist, P. D. & Rodenburg, J. M. Beyond the conventional information limit: the relevant coherence function. *Ultramicroscopy* **54**, 61–74 (1994).

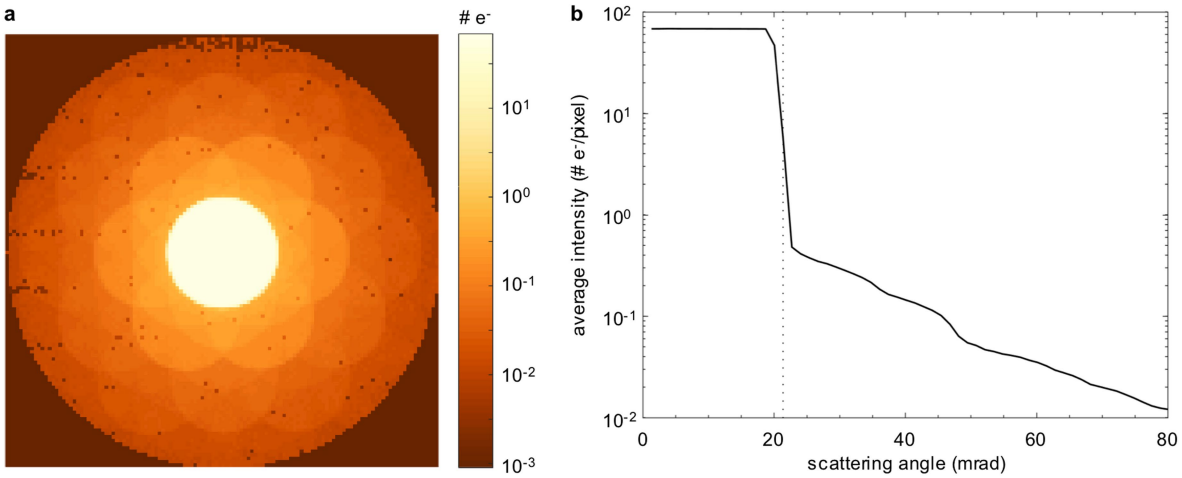

Extended Data Fig. 1 | Position-averaged diffraction pattern of the 4D dataset from monolayer MoS_2. a, Position-averaged convergent beam electron diffraction (CBED) pattern from the 4D dataset from monolayer MoS_2. **b**, Radially averaged intensity distribution (on a logarithmic scale) of the CBED pattern, showing the dynamic range spanned by the scattering distribution.

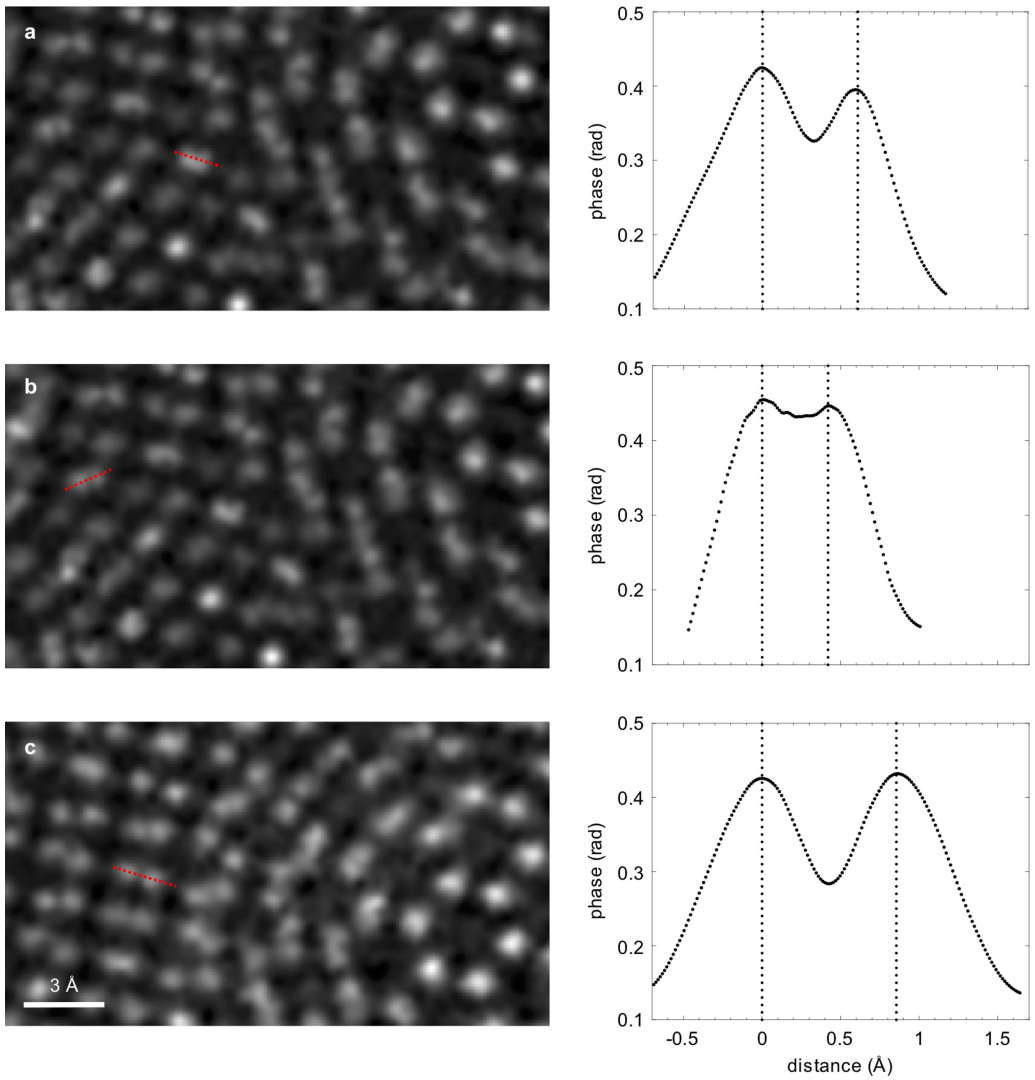

Extended Data Fig. 2 | Line profiles through atom pairs in the twisted bilayer MoS_2. Line profiles are from atom pairs in Fig. 3, with the respective subregions shown on the left. **a**–**c**, The measured peak–peak separations between two atoms are 0.42 ± 0.02 Å (**a**), 0.61 ± 0.02 Å (**b**) and 0.85 ± 0.02 Å (**c**).

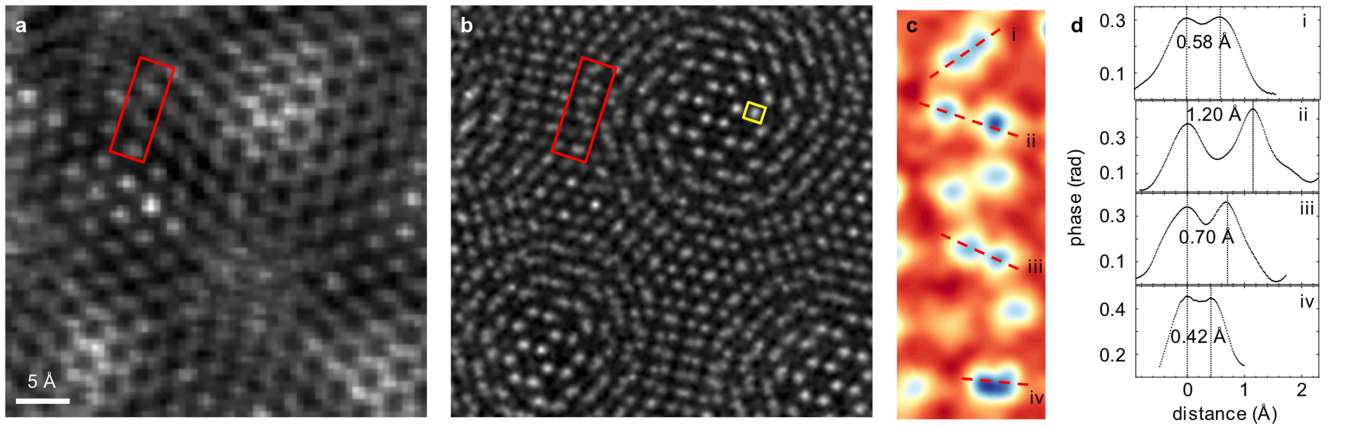

Extended Data Fig. 3 | ADF image and line profiles through atom pairs in the twisted bilayer MoS_2. a, ADF image synthesized from the 4D diffraction dataset. **b**, Phase of the transmission function reconstructed by ptychography. The yellow marker indicates a pair of atoms that is predicted to have a separation of 0.2 Å on the basis of the structural model, but cannot be resolved explicitly in our reconstruction. For a more detailed comparison, a red box is placed over corresponding regions in **a** and **b**. **c**, Enlarged image of the red boxed region in **b**, with the false colour scale of Fig. 3. **d**, Line profiles across the atom pairs labelled with dashed lines in **c**. The peak–peak separations are overlaid near the line profiles.

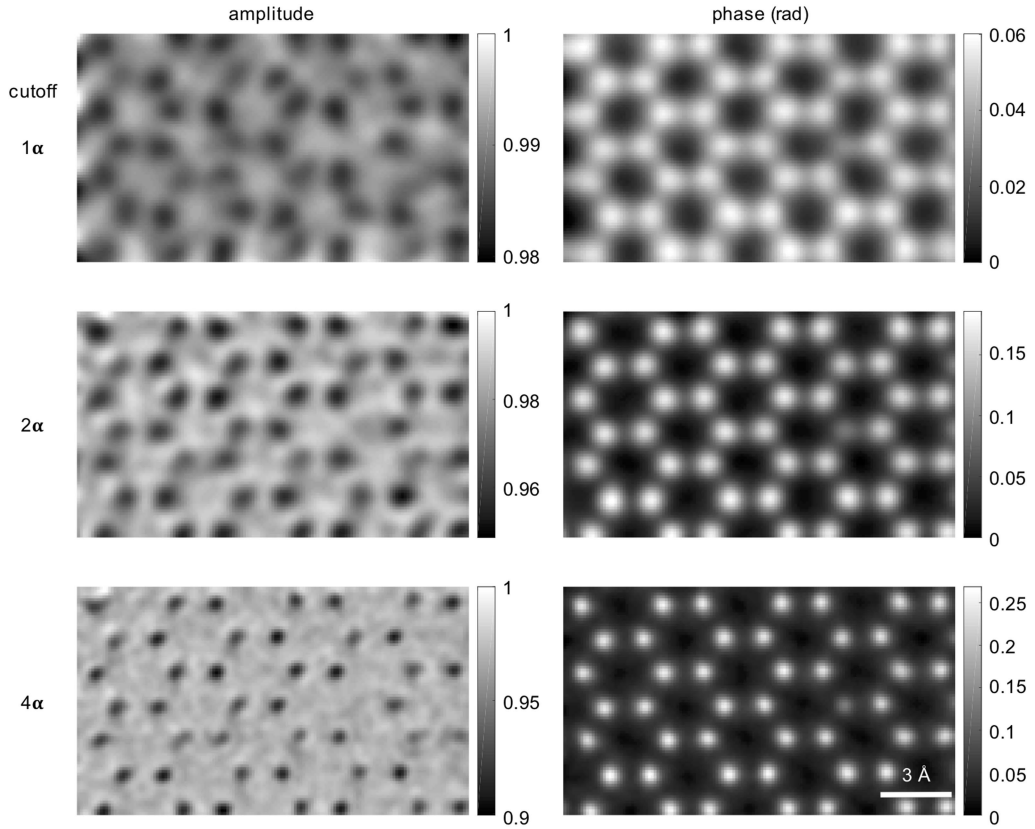

Extended Data Fig. 4 | Reconstructed amplitude and phase of monolayer MoS_2 at different cutoff angles. Both the amplitude (left panels) and phase (right panels) of the reconstructed transmission function show the atomic structure of monolayer MoS_2. Image resolution improves as the cutoff angle increases. Amplitude modulations are relatively weak, deviating by only a few per cent from a pure phase object (that is, an object function with unit amplitude).

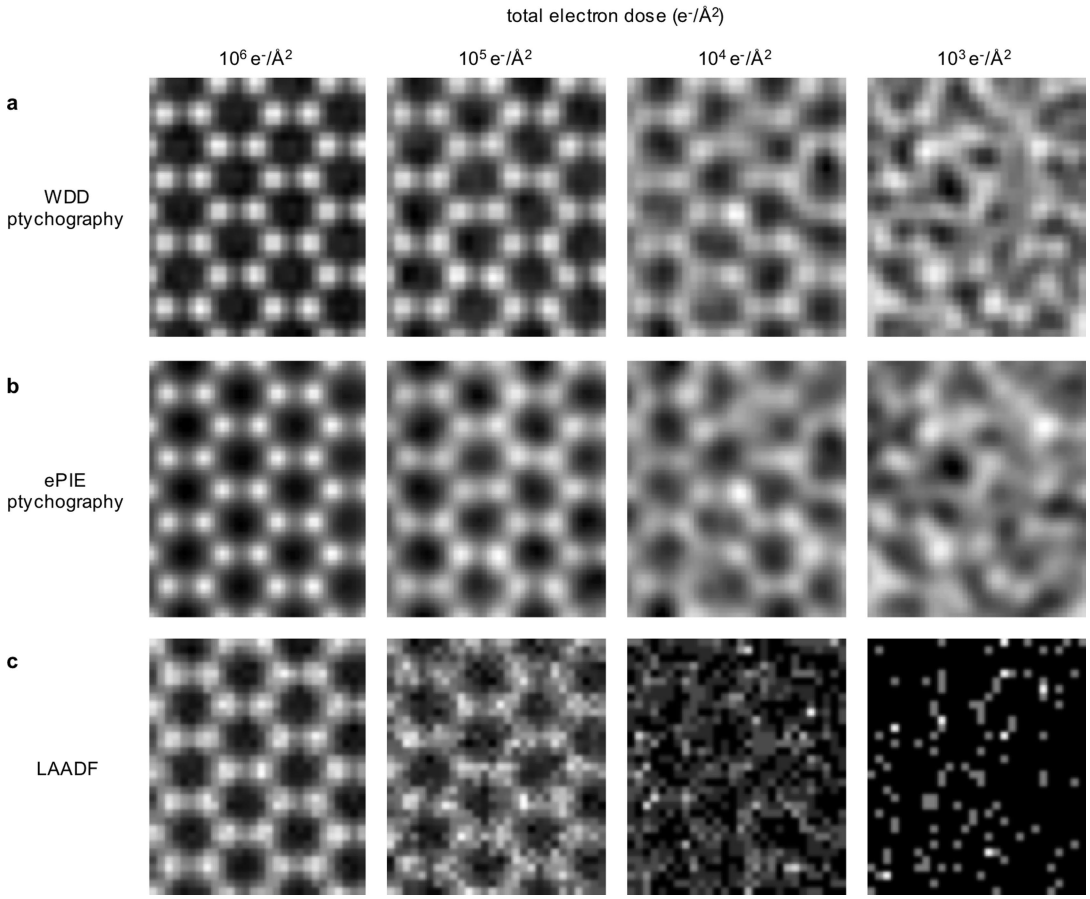

Extended Data Fig. 5 | Comparison between ptychography techniques and low-angle ADF imaging of graphene. a, **b**, Ptychographic reconstructions of simulated data with an in-focused probe, using the WDD (**a**) and ePIE (**b**) methods. **c**, Low-angle ADF (integrating from 1α to 4α) reconstruction using the same simulated datasets. Both ptychographic methods show similar reconstructions and are about 10 times more dose-efficient than the low-angle ADF technique. Beam energy, 80 keV; aperture size (α), 21.4 mrad.

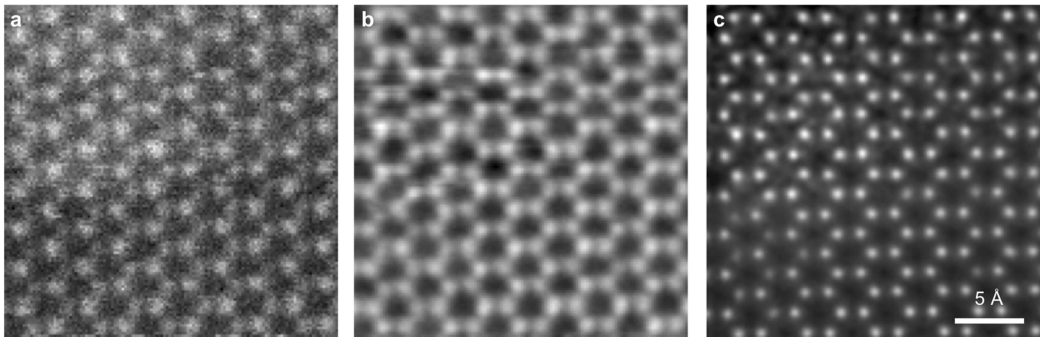

Extended Data Fig. 6 | Influence of scanning drift and contamination. **a**–**c**, ADF image (**a**), iCoM image (**b**) and phase of transmission reconstructed by full-field ptychography (**c**) using 128 × 128 diffraction patterns, covering a field of view of 2.7 nm × 2.7 nm. The ADF and iCoM reconstructions both suffer from stripe artefacts and large contrast variations. In the ptychographic reconstruction, scanning drift distorts and blurs reconstructed atoms in the vicinity of the scan distortion, but the overall resolution away from the distortion remains higher than the other imaging modes.

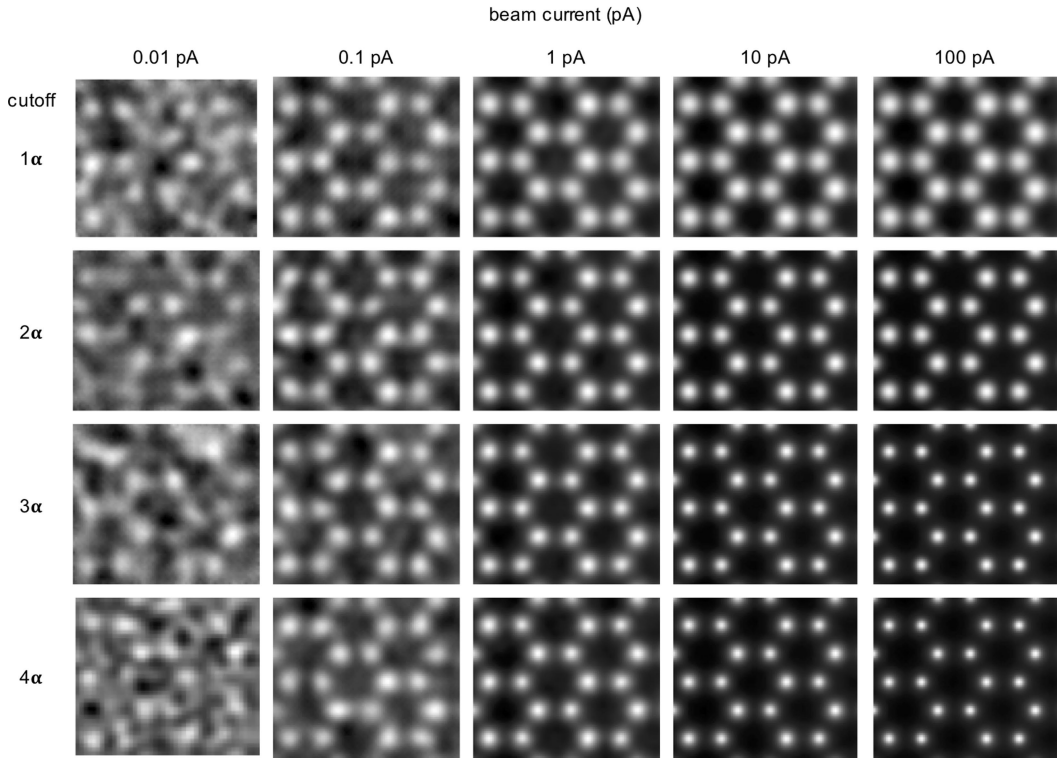

Extended Data Fig. 7 | Effect of dose and cutoff angles on ptychographic reconstructions of monolayer MoS_2 using simulated diffraction patterns. At high beam current, the resolution of the ptychography reconstruction is fundamentally determined by the collection angle of the detector. As the beam current decreases, the resolution becomes dose-limited and noise artefacts start to appear in the ePIE reconstruction. Beam energy, 80 keV; aperture size (α), 21.4 mrad.

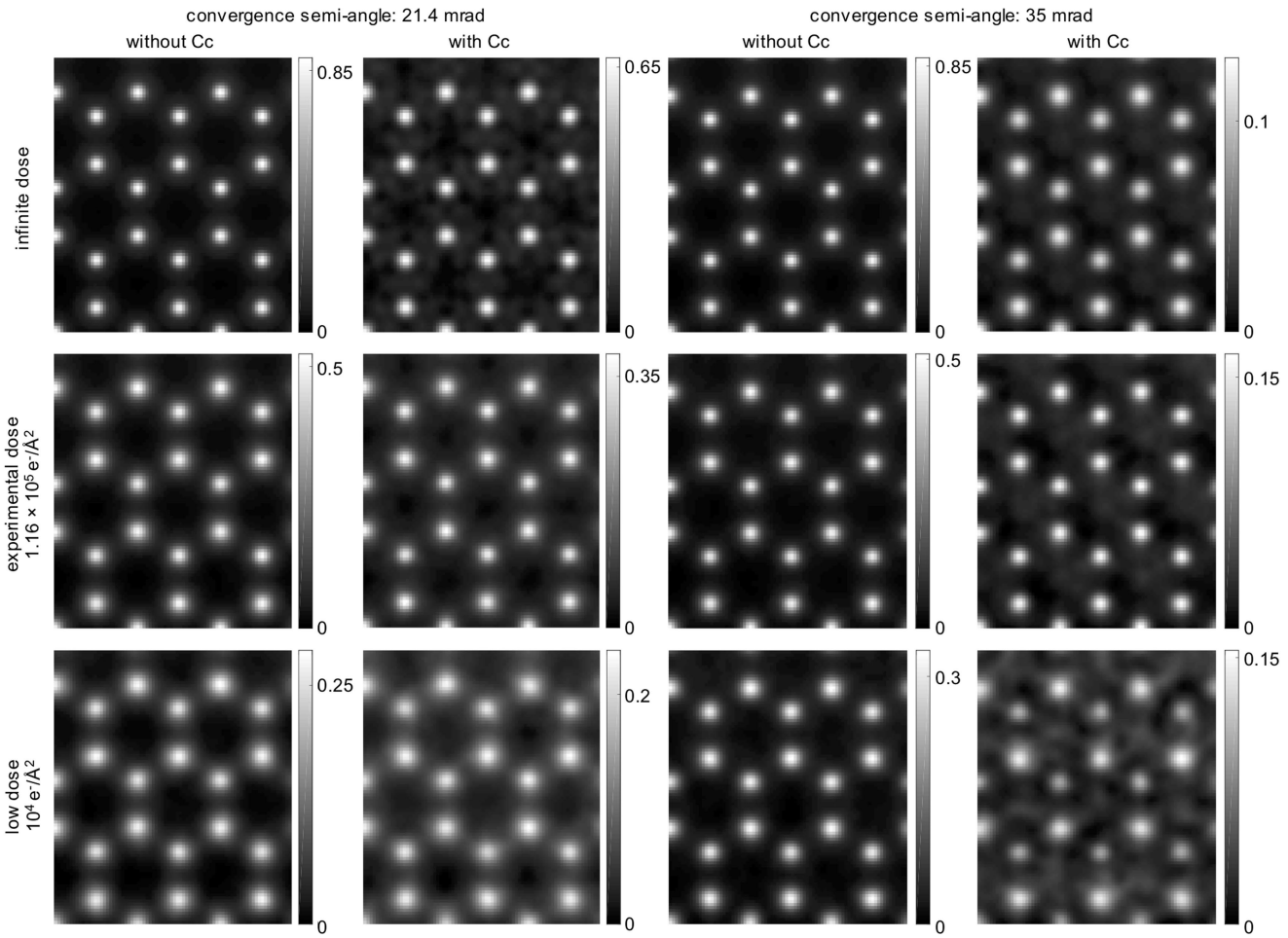

Extended Data Fig. 8 | Effect of chromatic aberrations at different electron doses for ptychographic reconstructions of monolayer MoS_2 using simulated datasets at 80 keV. Two convergence semi-angles are shown, 21.4 mrad (left two columns) and 35 mrad (right two columns), representing conditions under which chromatic aberrations have moderate and large effects on the incident probe shape, respectively ($C_c = 1.72$ mm, $\Delta E = 1.1$ eV). 21.4 mrad is also the experimental convergence angle. The incident electron dose levels are an infinite dose (top row), the experimental dose of 1.16×10^5 electrons per Å^2 (middle row) and a low dose of 10^4 electrons per Å^2 (bottom row). In the presence of noise, chromatic aberrations degrade the phase range of the reconstruction compared with the achromatic data. The data for the larger convergence semi-angle are more strongly affected. At infinite and experimental doses, ptychographic reconstructions with and without chromatic aberration are visually similar for both convergence angles. At low dose and with chromatic aberration, the reconstructed atoms are broadened, and distinct artefacts appear for a convergence angle of 35 mrad.